Advances in Aircraft and Spacecraft Science, *Vol. 6, No. 1 (2019) 69–86*
DOI: https://doi.org/10.12989/aas.2019.6.1.069

Full field strain measurements of composite wing by digital image correlation

A. Pagani*[1], E. Zappino[1a], A.G. de Miguel[1b], V. Martilla[2c] and E. Carrera[1d]

[1]MUL[2] group, Department of Mechanical and Aerospace Engineering, Politecnico di Torino, Turin, Italy
[2]C.F.M. Air s.r.l., Cirié, Turin, Italy

(Received July 30th, 2018, Revised September 18th, 2018, Accepted September 19th, 2018)

Abstract. This paper discusses the use of the Digital Image Correlation (DIC) technique for the displacement and strain measurements of a wet lay-up composite wing. As opposed to classical strain gages, DIC allows to conduct full field strain analysis of simple to complex structural parts. In this work, wing-up bending tests and measurements of the composite wing of the Dardo Aspect by CFM Air are carried out through an ad-hoc test rig and the Q-400 DIC system by Dantec Dynamics. Also, the results are used to validate a finite element model of the structure under investigation.

Keywords: digital image correlation; composite wings; full field strain analysis

1. Introduction

Over the last few decades, the rapid growth in computational analysis has substantially facilitated new techniques in experimental mechanics. Among these, Digital Image Correlation (DIC) has emerged as a leading technology in structures and materials characterization (Daly 2010). DIC is a non-contact, optical methodology that employs tracking and image registration techniques for accurate 2D and 3D measurements of changes in images. This method is used to measure full field, three-dimensional displacements and superficial strains. Compared to strain gages and extensometers, the amount of information gathered about the fine details of deformation during mechanical tests is increased manyfold.

DIC was used for the first time to measure the in-plane deformations on a planar object by Peters and Ranson (1982) and Sutton *et al.* (1983). Extension to 3D objects was then proposed in several works in the early 1990s, see for example Luo *et al.* (1993) and Helm *et al.* (1996). Here, two or more cameras are utilized to simultaneously capture the out-of-plane displacements. DIC technology is thus employed to correlate the two images acquired from the cameras. Also, in order to track and

*Corresponding author, Assistant professor, E-mail: alfonso.pagani@polito.it
[a]Assistant professor, E-mail: enrico.zappino@polito.it
[b]Ph.D. student, E-mail: alberto.garcia@polito.it
[c]Dr., Head of technical office
[d]Professor, E-mail: erasmo.carrera@polito.it

http://www.techno-press.org/?journal=aas&subpage=7 ISSN: 2287-528X(Print), 2287-5271(Online)

triangulate the progressive deformation from the initial configuration, a calibration procedure must be performed for determining the relative position of the two cameras. Calibration is generally made by using a set of images with a pre-determined pattern (Schreier *et al.* 2004).

The accuracy of DIC measurements is highly affected by the quality of the surface pattern. In fact, measured objects must have a non-periodic and high-contrast surface pattern in order to guarantee the uniqueness of the image tracking procedure. Many papers in the literature have provided guidelines for surface preparation, see for example the work by Chu *et al.* (1985). Of course, the surface pattern should not alter the mechanical characteristics of the measured objects. Furthermore, it has been shown that smooth transition from black and white is preferable for accurate acquisitions and that oversampling must be avoided by using an opportune ratio between the camera's pixels and the pattern density.

Nowadays, DIC is an accessible and mature technology which is constantly applied in many engineering fields, including civil engineering for analysis (Sozen 2015, Dai *et al.* 2017, Felekoglu and Keskinateş 2016) and monitoring (Aggelis *et al.* 2016). Regarding aerospace engineering, Vialettes *et al.* (2006) employed DIC to measure the strain fields over the surface of of long duration super-pressure balloon in realistic flight conditions. Stanford *et al.* (2008) employed 3D DIC to measure geometry, displacements, and plane strains of a fixed membrane wings for micro air vehicles. Also, DIC and photogrammetry continue to be used at NASA Langley Research Center's (LaRC) Landing and Impact Research Facility (LandIR) for the characterization of full-scale aircraft crash testing (Littell 2016). Apparently, the interest of the aerospace research community on DIC technology is vivid, but its application to certification of aerospace structures is still problematic. The main reason is that a necessary requirement for certification tests is that all the instrumentation employed is properly calibrated. In DIC, although camera calibration is used, no accepted procedure is available as yet to calibrate the displacement and strain fields. On this topic, extensive work is still demanded from scientists and engineers.

The present paper shows an exercise on the use of 3D DIC for the strain and displacement measurements of a wet lay-up composite wing. The paper is organized as follows: (i) Section 2 introduces the experimental set-up and the composite wing under consideration; (ii) the analysis and the full field displacements and strains of different parts of the wing are, thus, shown in Section 3, along with a validation against a finite element model; (iii) finally, the main conclusions are discussed in Section 4.

2. Experimental apparatus

Figure 1 shows the primary structure of the *Dardo Aspect* in CFM Air hangar in Cirié, Torino, Italy. Dardo is a wet-laminate full composite aircraft designed for low-cost, high efficiency military screener and initial trainer. The maximum take-off weight is $W = 700$ kg, the wing-span is $b = 8.4$ m, and the aircraft length is $L = 7$ m. In this work, strain measurements of the composite wing are described. The test article was, thus, attached to the test rig so as to accurately simulate the wing connection to the fuselage, see Fig. 2. The load is applied through an hydraulic piston and with no feed-back signal, for reasons of simplicity. The *wing-up bending test* is realized by distributing the piston load at the location of the ribs via a whiffle tree.

The DIC instrument equipped for the tests is a Q-400 DIC system by Dantec Dynamics, whose optical features allow to measuring true full field, non-contact and three-dimensional shape, displace-

Figure 1 Primary composite structure of CFM Air Dardo Aspect

ments and strains on components and structures made from almost any material. The Q-400 system can be used for determination of three-dimensional material properties in tensile, torsion, bending or combined tests. This apparatus, essentially, is made of two 2-megapixel cameras for high-resolution and high-frequency image tracking, one led lamp, the supporting structure, the data acquisition unit, and the calibration tool. Image processing, on the other hand, is performed with the licensed Instra4D V2.1 software tool. The Q-400 system is shown in Fig. 3 during preliminary set-up in the laboratories of Politecnico di Torino. In contrast, Fig. 4 shows the calibration phase of the Q-400 DIC system during data acquisition in CFM hangar.

3. Full field strain analysis

3.1 Preliminaries

The measurements of true full field displacements and strains of three different areas of the test article were performed during three separate loading phases, from 0% to approximately 120% of the limit load. These three areas are located as follows:

- Test area 1. Spar web at wing root.
- Test area 2. Spar cap at wing root.
- Test area 3. Second-bay top skin.

The test area number 1 is placed on the spar web, close to the wing root. The exact location of the area is shown in Fig. 5, where a front view of the current wing design is depicted and the measured area is red colour. In contrast, Fig. 6 shows the exact location of the test area 2, which is placed on the main spar cap, close to the wing symmetry plane. Fig. 7 shows areas 1 and 2 after surface treatment, which consisted in painting a random pattern on a contrast background by spray painting. This treatment allowed for accurate image tracking and deformation/displacements measurements,

as it will be discussed in the next section. For completeness reasons, Figs. 8 and 9 show, respectively, the placement and the superficial treatment of test area 3, which is placed on the second-bay top skin.

Figure 2 Experimental set-up

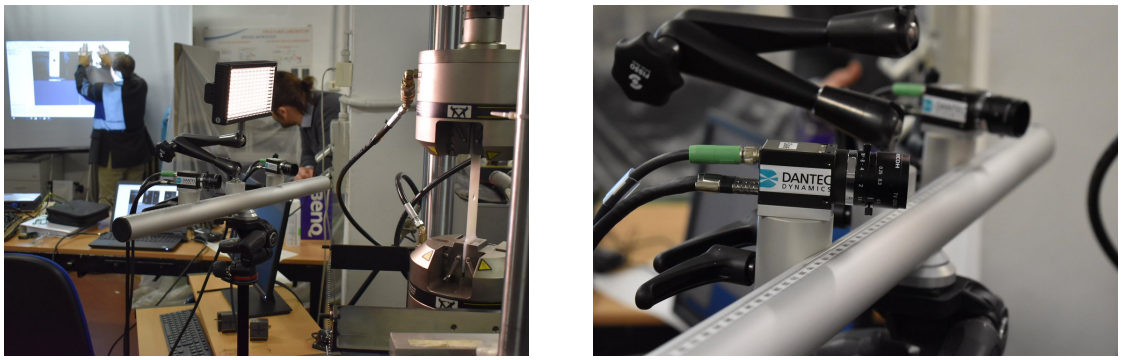

(a) (b)

Figure 3 Digital 3D Image Correlation System Q-400 by Dantec Dynamics during set-up

Figure 4 Calibration of Q-400 DIC system in CFM hangar

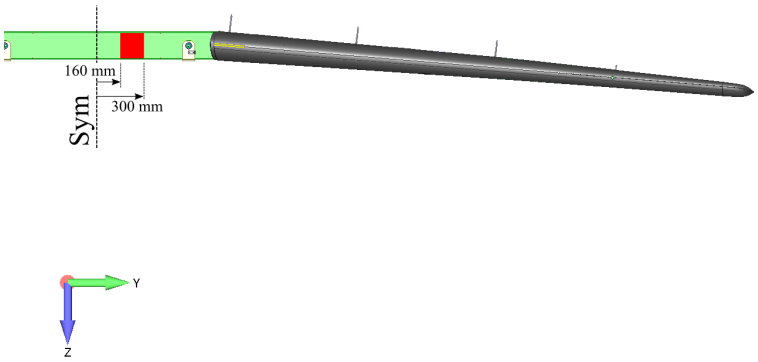

Figure 5 Front view of the composite wing. Test area 1 in red. Spar web at the wing root

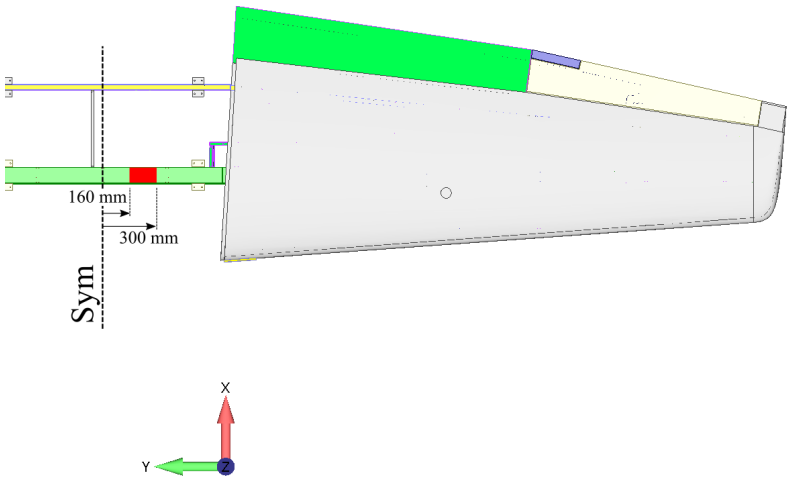

Figure 6 Top view of the composite wing. Test area 2 in red. Spar cap at wing root

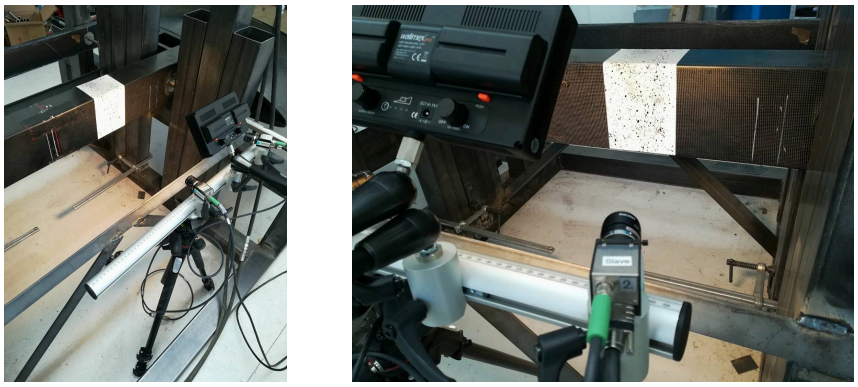

(a) (b)

Figure 7 Test areas 1 and 2 (main spar) after superficial treatment and during image acquisition

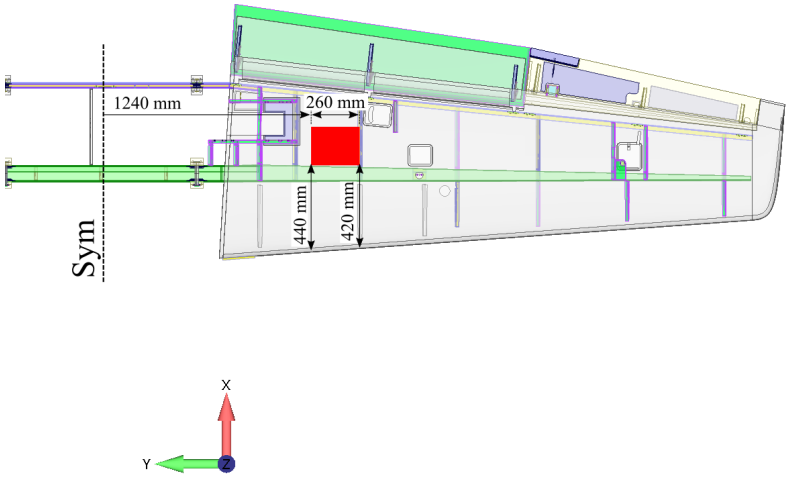

Figure 8 Top view of the composite wing. Test area 3 in red. Second-bay top skin

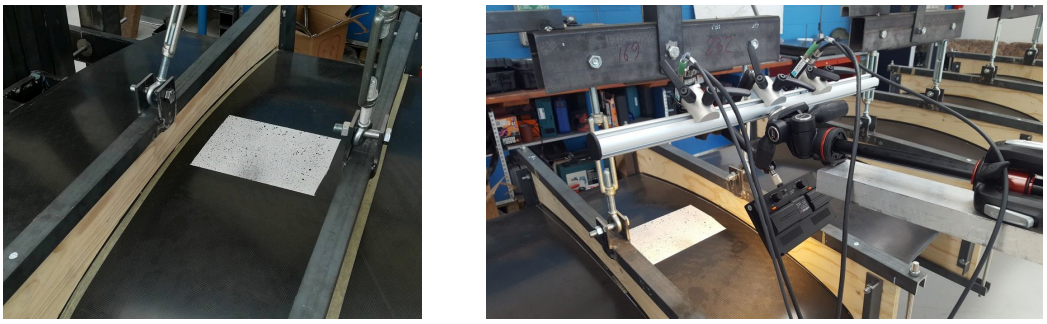

(a) (b)

Figure 9 Test area 3 (top panel) after superficial treatment and during image acquisition

Table 1 quotes the applied load steps during DIC acquisition of images on test areas 1 to 3. It is important to underline that the mass of the wing plus the supports at the location of the ribs is applied at load step 1, which means 0% of the limit load. In other words, the wing is - in principle - free of stresses at load step 1.

Table 1 Loadings applied during DIC measurements

Load step	Perc. of limit load [%]	Tot. applied load [kgf]	Wing net load [kgf]
1	0	886	152*
2	20	1243	330
3	40	1602	510
4	60	1962	690
5	80	2318	868
6	100	2675	1045**
7	120	3034	1226

*Mass of wing + ribs supports is 152 kg **Limit load is 895 kgf

3.2 Best fit plane

Figure 10 shows the distance from the best fit plane of the virtual acquisition points on areas 1, 2 and 3. The results that follow are given in terms of a Cartesian reference frame whose xy-plane lays on the best fit plane of each measured area. From the pictures it is clear that the measured areas are not perfectly planar. This was expected for test area 3, of course, as wing panels are curved. Non-null distances from the fitting plane for test areas 1 and 2, instead, denotes small manufacturing uncertainties, of the order of tenths of a millimeter.

3.3 Analysis of the main spar web at wing root

DIC measurements of displacement and strain components on test area number 1 are summarized in this section. The results of the acquisitions are shown in Fig. 11. This figure shows the distributions of in-plane (u_x and u_y) and out-of-plane (u_z) displacement components, in-plane tangential (ϵ_{xx} and ϵ_{yy}) and shear (ϵ_{xy}) true strains, as well as principal true strains (ϵ_{11} and ϵ_{22}) for a loading condition equal to approximately 100% of limit load. Note that ϵ_{xx} is linear along y, whereas ϵ_{xy} is nearly null (shear load is zero along the spar at wing root).

For the sake of completeness, Fig. 12 shows the mean transverse displacement component along y all along the test load steps. Finally, Fig. 13 shows the distribution of the in-plane strain component ϵ_{xx} along the y direction for load step 6. Strains from DIC measurements are given in millistrain (mstrain $=$ strain $\times 10^3$). It must also be underlined that the coordinate reference system is defined so that the xy-plane is indeed the best fit plane of the pattern on the surface of test area. Note that Fig. 12 shows a mechanical backlash of the test rig between load steps 1 and 2, which does not affect the validity of the present analysis.

3.4 Analysis of the main spar cap at wing root

Analogously to the previous section, DIC measurements of displacement and strain components on test area number 2 are summarized hereinafter. The results of the acquisitions are summarized in Fig. 14, which shows distribution of important displacements and strains on the measured area for wing net load equal to 1045 kgf ($\approx 100\%$ of limit load). Note that ϵ_{xx} is approximately constant on the spar cap (bending moment is constant at the wing root). In contrast, Fig. 15 shows the mean values of the three in-plane strain components for different load steps.

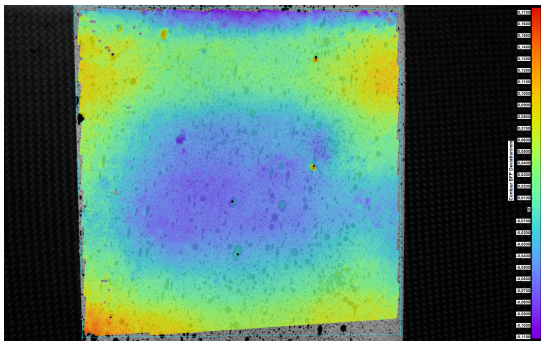

(a) Test area 1

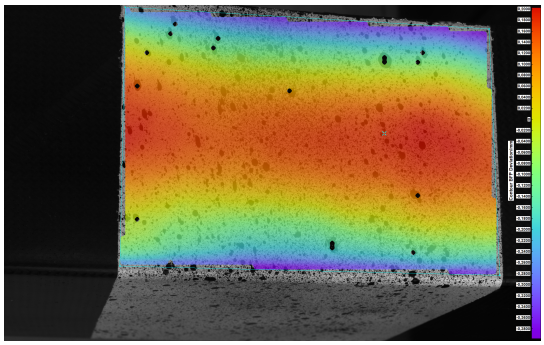

(b) Test area 2

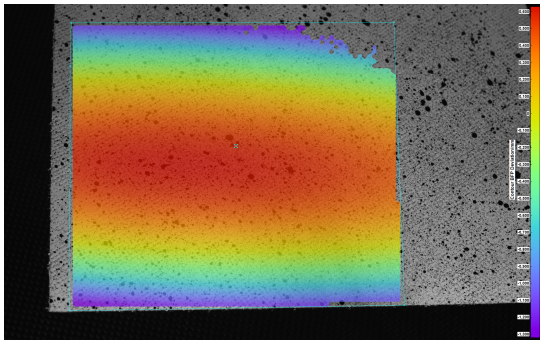

(c) Test area 3

Figure 10 Distance from best fit plane

As a final remark, note that the results are given in terms of a Cartesian coordinate system whose xy-plane lays on the best fit plane on test area 2. In other words, the coordinates of this system are different from those of test area 1 and test area 3, which follow in the next sections.

3.5 Analysis of the second-bay top skin

The results from the acquisition of strain and displacements on the second-bay top skin are finally presented in this section. These results, in detail, are shown in Fig. 16 for load step 6. Moreover, Figs. 17 and 18 show the mean values of the transverse displacement along z and the three strain components for all the load steps, respectively. Nevertheless, it must be underlined that, in this case, the in-plane strain component ϵ_{xx} is not constant over the acquisition domain, but linear along x (see Fig. 19), because the bending moment is piecewise linear along the wing axis.

3.6 Validation

For the reasons of completeness, DIC results are briefly compared with a mathematical model in this section. For this purpose, a Finite Element Model (FEM) of the composite wing of Dardo is built and analysed by using Nastran (MSC.Software 2010). The model is depicted in Fig. 20, where loadings and boundary conditions are also shown. Loadings are applied in correspondence of the ribs

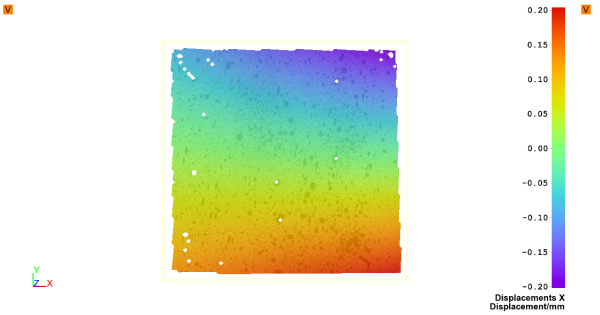

(a) In-plane displacements along x

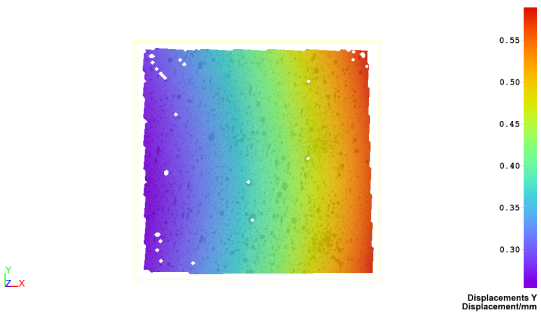

(b) In-plane displacements along y

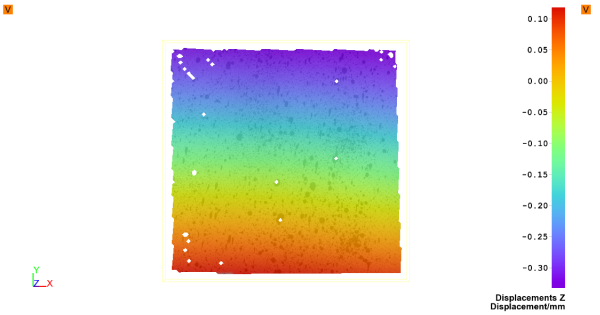

(c) Out-of-plane displacements along z

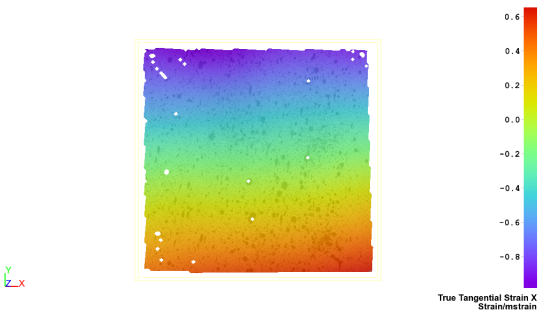

(d) True strain ϵ_{xx}

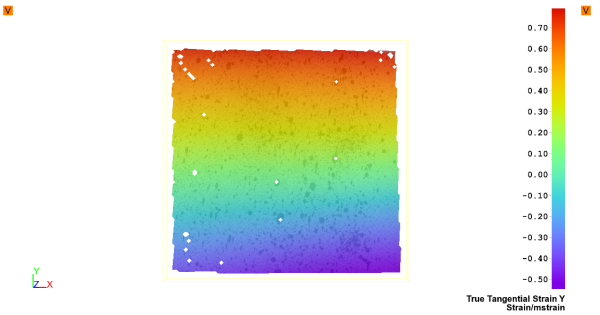

(e) True strain ϵ_{yy}

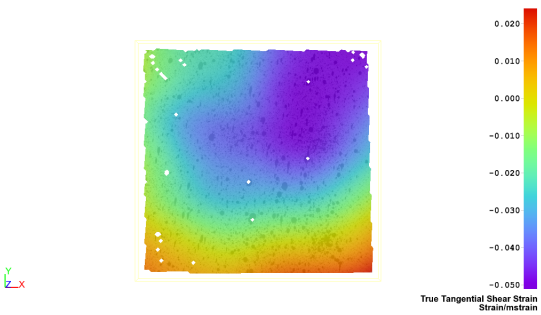

(f) True strain ϵ_{xy}

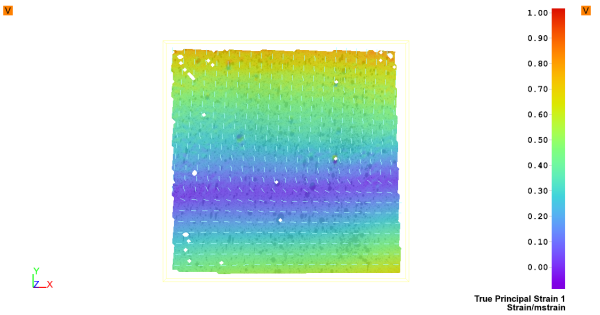

(g) Principal true strain ϵ_{11}

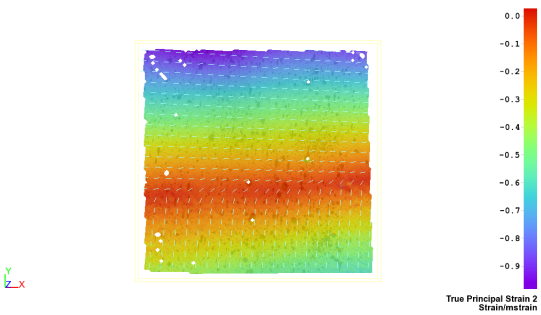

(h) Principal true strain ϵ_{22}

Figure 11 Full field displacements and strains on test area 1, main spar web at wing root. Wing net load is 1045 kgf; i.e., approximately 100% of limit load

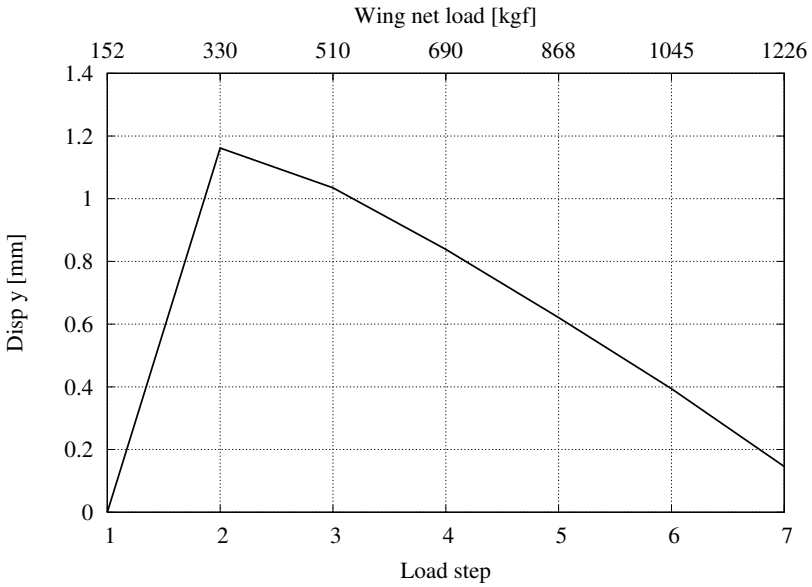

Figure 12 Mean transverse displacement along y of test area 1, main spar web at wing root

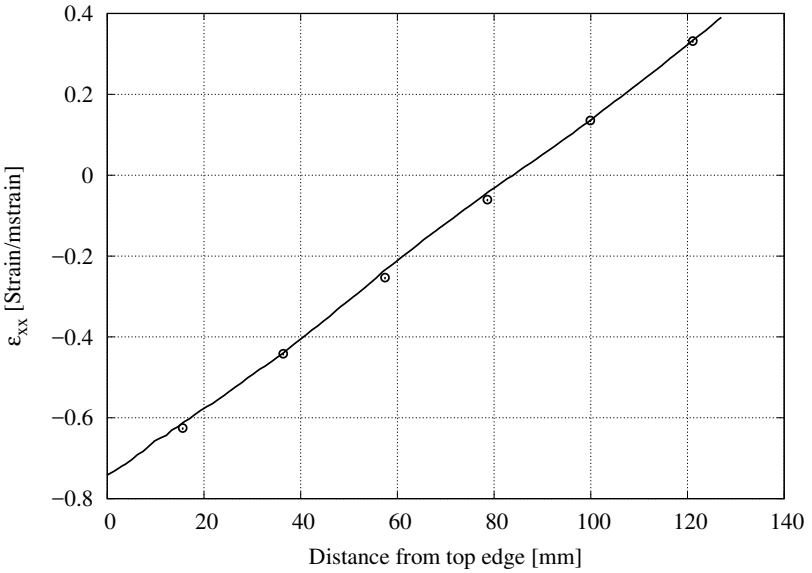

Figure 13 Distribution of ϵ_{xx} along y direction for main spar web at wing root. Wing net load is 1045 kgf; i.e., approximately 100% of limit load. Circles "$\circ$" represent FEM results

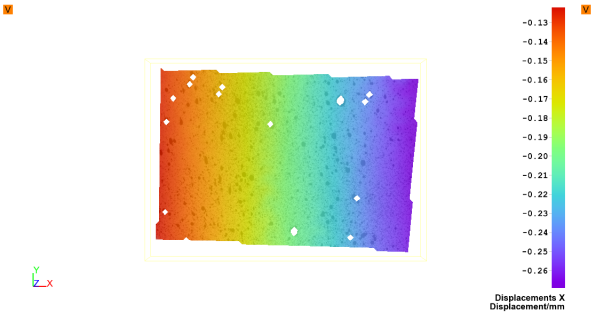

(a) In-plane displacements along x

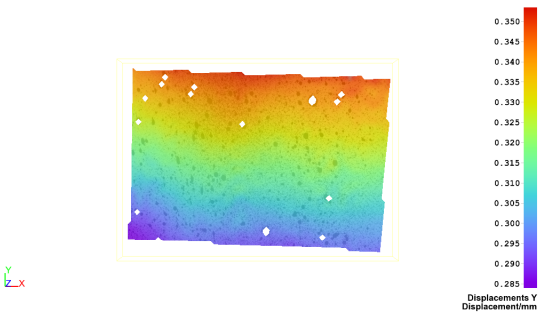

(b) In-plane displacements along y

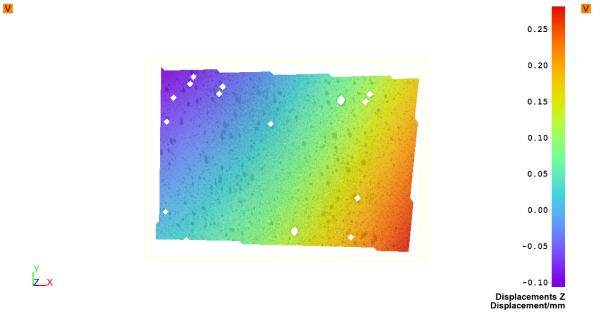

(c) Out-of-plane displacements along z

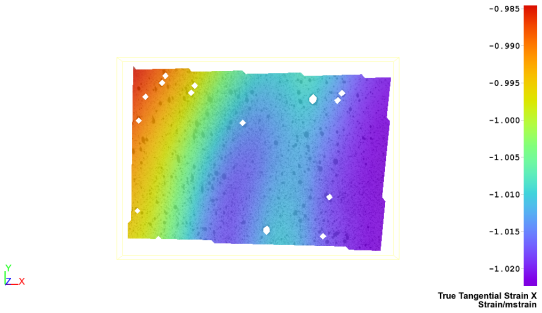

(d) True strain ϵ_{xx}

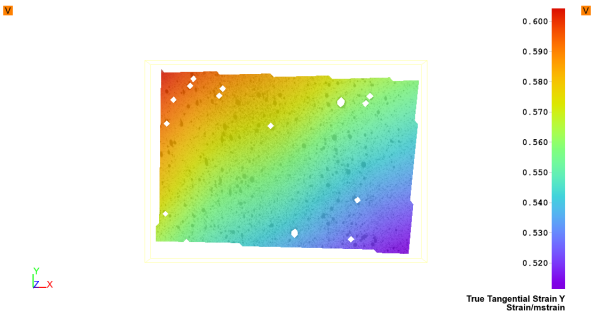

(e) True strain ϵ_{yy}

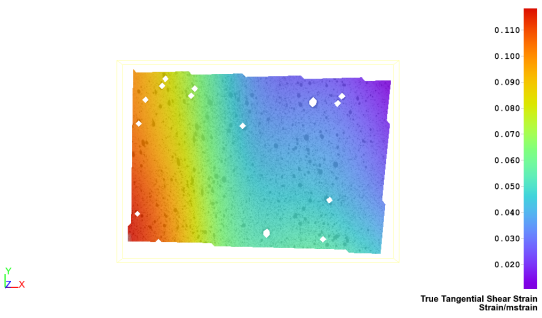

(f) True strain ϵ_{xy}

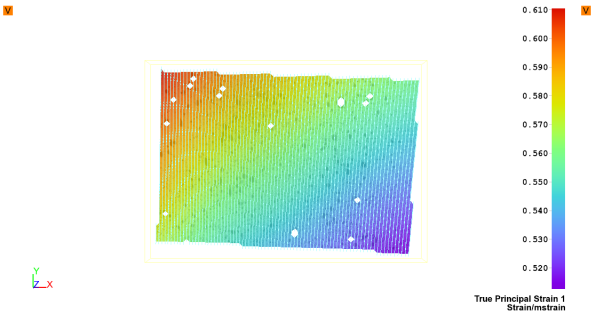

(g) Principal true strain ϵ_{11}

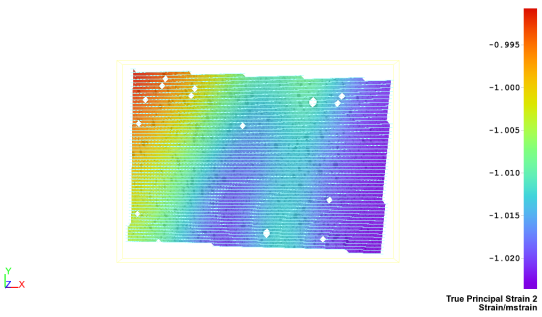

(h) Principal true strain ϵ_{22}

Figure 14 Full field displacements and strains on test area 2, main spar cap at wing root. Wing net load is 1045 kgf; i.e., approximately 100% of limit load

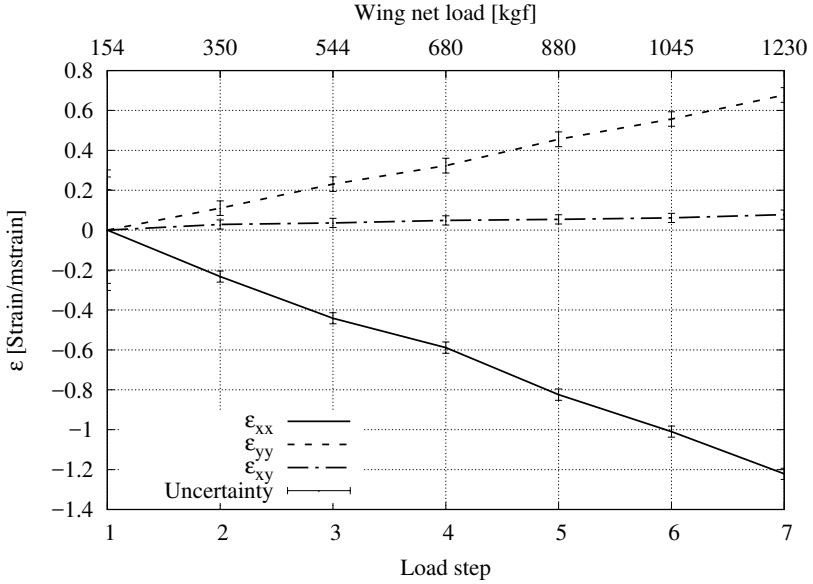

Figure 15 Mean strain components of test area 2, main spar cap at wing root

so as to simulate the experiments accurately. The total applied load equals the limit load as in Table 1. Symmetry boundary conditions as well as fuselage attachments are simulated. The FEM model has a total of 26832 nodes and 27633 elements, including CQUAD plate as well as CBEAM elements. Details on the material and lamination are not given for brevity and reasons of confidentiality.

Comparison of important strain components between FEM model and DIC measurements on test area 1 (main spar web at wing root) is shown in Figs. 21 and 22. The former figure shows contour maps of the normal ϵ_{xx} strain component. In contrast, distribution of ϵ_{yy} is shown in Fig. 22. Additionally, the distribution of ϵ_{xx} along the in-plane vertical coordinate through the spar web is shown in Fig. 13. The results show a good correspondence between the FEM model and DIC. Slight differences due to uncertainty on the position of the measured areas and applied net load do not affect the validity of the analysis.

4. Conclusions

This paper has discussed the use of Digital Image Correlation (DIC) methodology for the full field displacement and strain measurements of a composite wet lay-up wing subjected to bending. The experimental set up consisted into an ad-hoc test rig, a load piston, and a Q-400 DIC system by Dantec Dynamics. After surface treatment and system calibration, several quasi-static loadings have been applied from 0% to approximately 120% of the limit load. Results from DIC acquisitions have been documented in terms of both displacements and in-plane strains. In addition, comparisons with a finite element model have been provided and the good agreement between test and numerical results was confirmed. To conclude, the resulting accuracy, reliability and practicability of the DIC application for aerospace structures confirm this technology as an enabling practice for continuous full field displacement and strain measurements.

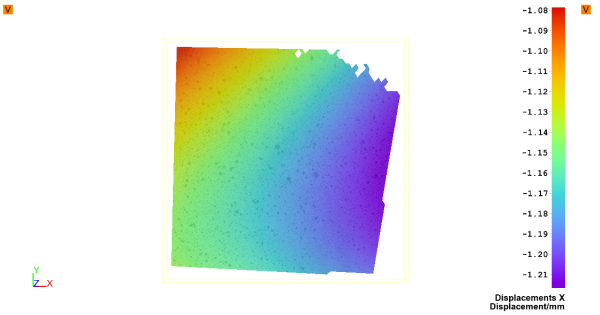

(a) In-plane displacements along x

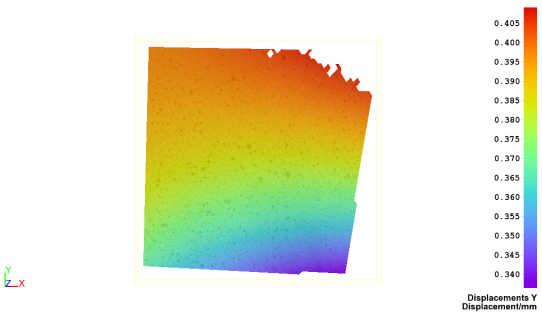

(b) In-plane displacements along y

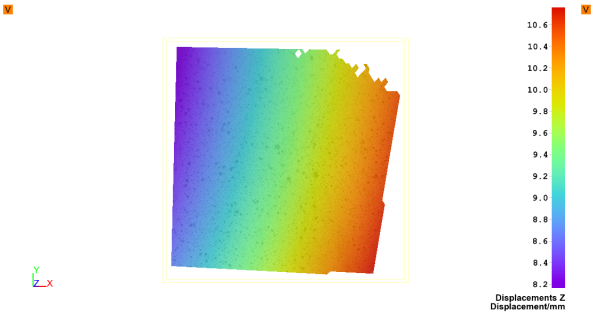

(c) Out-of-plane displacements along z

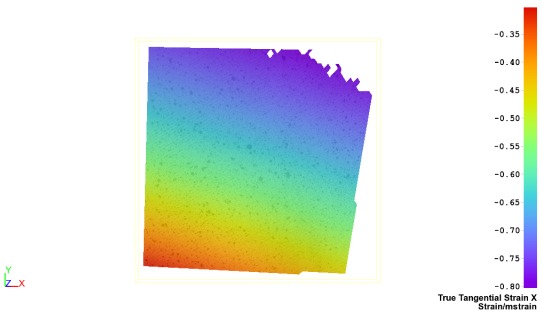

(d) True strain ϵ_{xx}

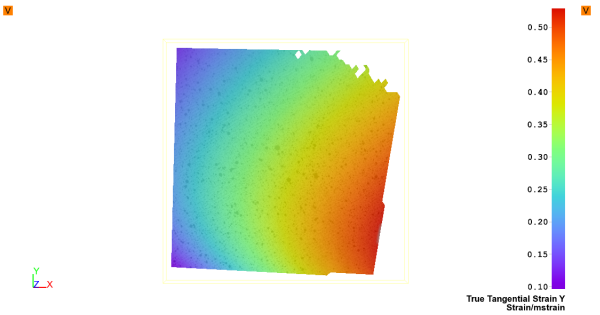

(e) True strain ϵ_{yy}

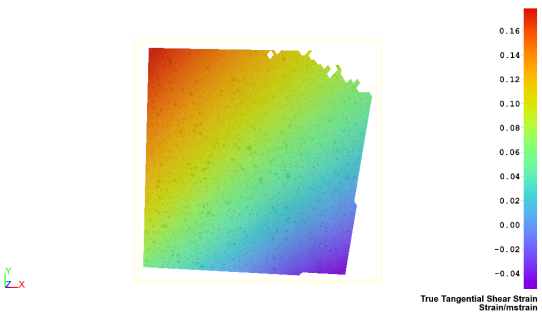

(f) True strain ϵ_{xy}

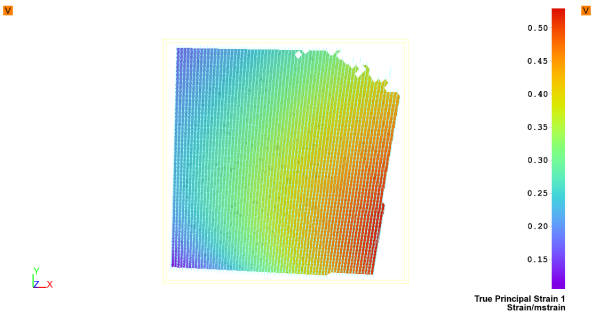

(g) Principal true strain ϵ_{11}

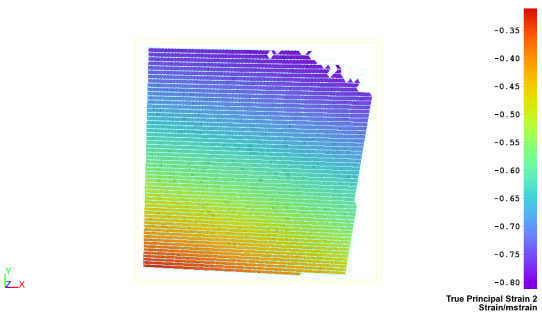

(h) Principal true strain ϵ_{22}

Figure 16 Full field displacements and strains on test area 3, second-bay top skin. Wing net load is 1066 kgf; i.e., approximately 102% of limit load

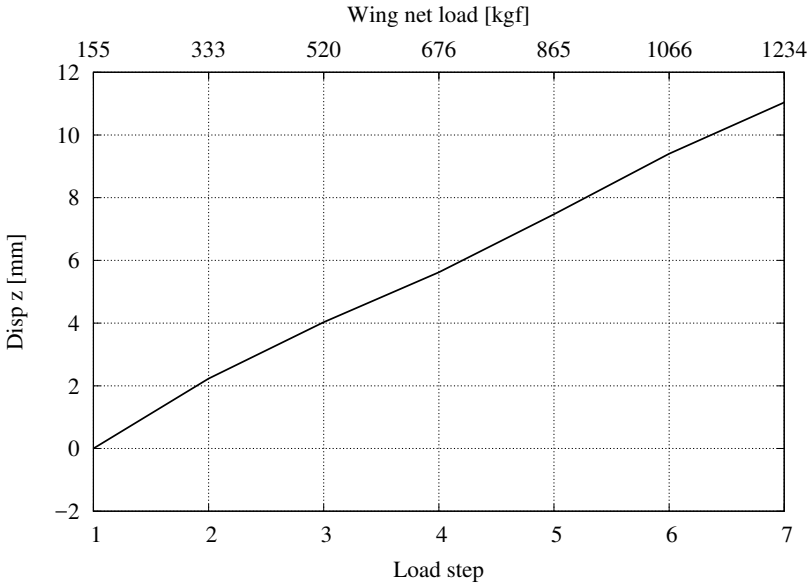

Figure 17 Mean transverse displacement along z of test area 3, second-bay top skin

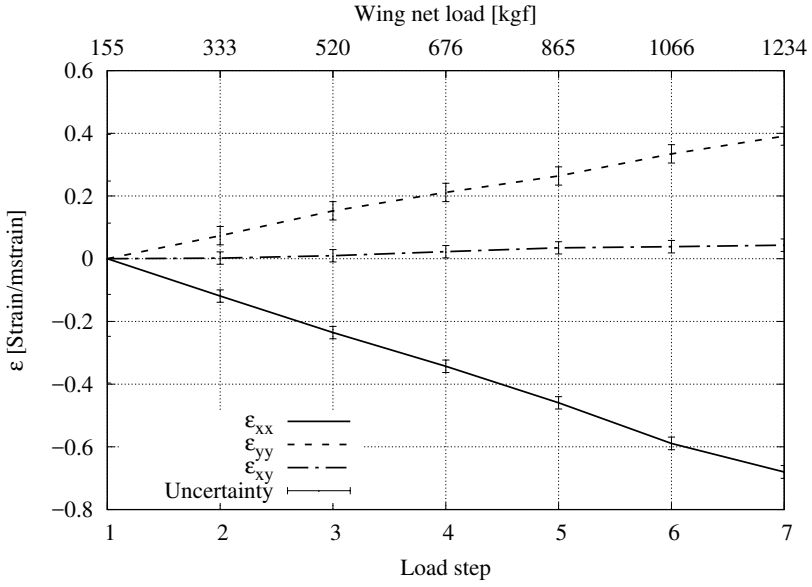

Figure 18 Mean strain components of test area 3, second-bay top skin

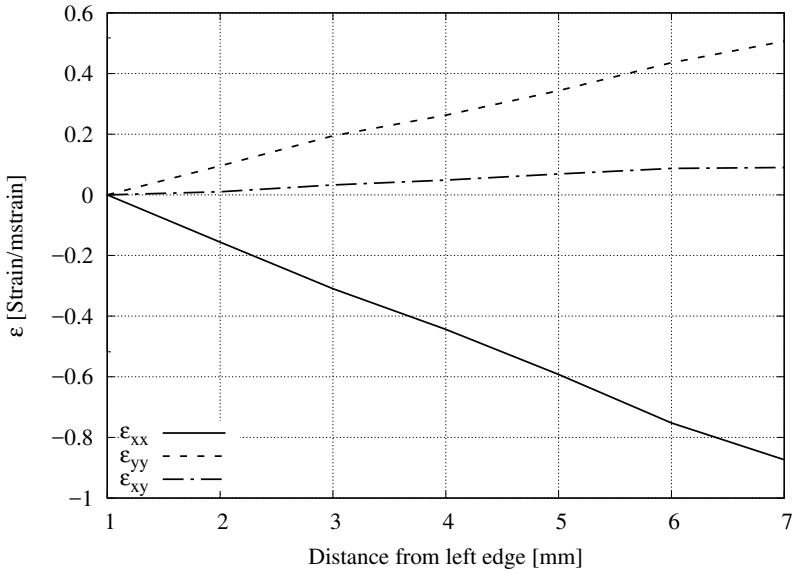

Figure 19 Distribution of strain components along x direction for load step 6 and test area 3, second-bay top skin

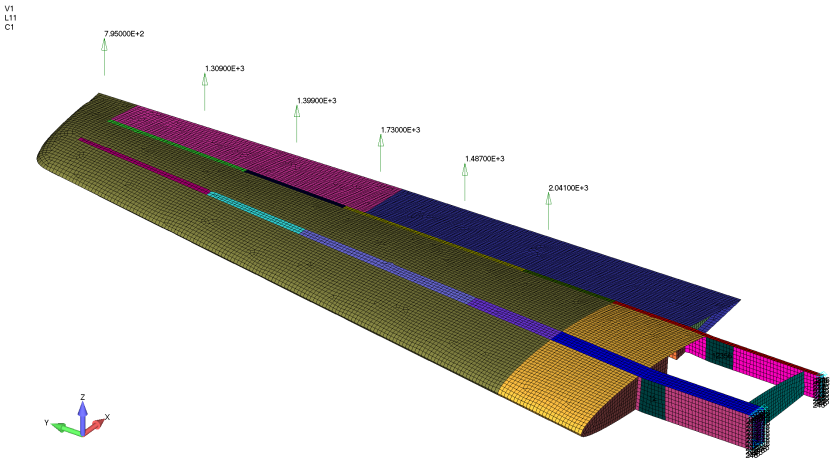

Figure 20 Finite element model of the composite wing

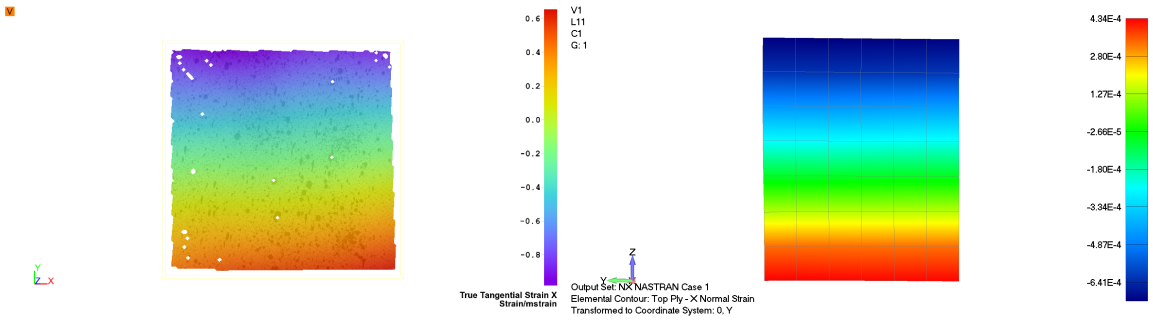

(a) DIC (b) FEM

Figure 21 Comparison between DIC and FEM. True strain ϵ_{xx} on test area 1, main spar web at wing root. Wing net load is 1045 kgf; i.e., approximately 100% of limit load. Note that DIC results are given as microstrains ($\times 10^3$)

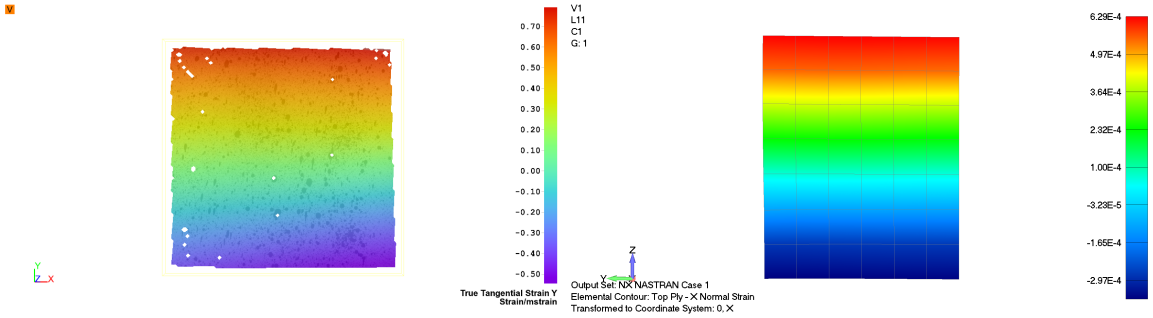

(a) DIC (b) FEM

Figure 22 Comparison between DIC and FEM. True strain ϵ_{yy} on test area 1, main spar web at wing root. Wing net load is 1045 kgf; i.e., approximately 100% of limit load. Note that DIC results are given as microstrains ($\times 10^3$)

Acknowledgements

This research has been co-funded by Embraer S.A. The first author also acknowledges financial support from the Compagnia di San Paolo through the project ADAMUS.

References

Aggelis, D.G., Verbruggen, S., Tsangouri, E., Tysmans, T. and Hemelrijck, D.V. (2016), "Monitoring the failure mechanisms of a reinforced concrete beam strengthened by textile reinforced cement using acoustic emission and digital image correlation", *Smart Struct. Syst.*, **17**(1), 91-105.

Chu, T.C., Ranson, W.F. and Sutton, M.A. (1985), "Applications of digital-image-correlation techniques to experimental mechanics", *Exper. Mech.*, **25**(3), 232-244.

Dai, Y.T., Wang, H., Ge, T.Y., Wu, G., Wan, J.X., Cao, S.Y., Yang, F.J. and He, X.Y. (2017), "Behavior Investigation of CFRP-Steel Composite Members Using Digital Image Correlation", *Steel Compos. Struct.*, **23**(6), 129-132.

Daly, S.H. (2010), *Digital Image Correlation in Experimental Mechanics for Aerospace Materials and Structures*, Encyclopedia of Aerospace Engineering, John Wiley & Sons, 1-11.

Felekoglu, B. and Keskinateş, M. (2016), "Multiple cracking analysis of HTPP-ECC by digital image correlation method", *Comput. Concrete*, **17**(6), 831-848.

Helm, J.D., McNeill, S.R. and Sutton, M.A. (1996), "Improved three-dimensional image correlation for surface displacement measurement", *Optic. Eng.*, **35**, 1911-1921.

Littell, J.D. (2016), *Experimental Photogrammetric Techniques Used on Five Full-Scale Aircraft Crash Tests*, Technical Report TM-2016-219168, NASA.

Luo, P.F., Chao, Y.J., Sutton, M.A. and Peters, W.H. (1993), "Accurate measurement of three-dimensional deformations in deformable and rigid bodies using computer vision", *Exper. Mech.*, **33**, 123-132.

MSC.Software (2010), *MD/MSC Nastran 2010 Quick Reference Guide*.

Peters, W.H. and Ranson, W.F. (1982), "Digital imaging techniques in experimental stress analysis", *Opt. Eng.*, **21**(3), 213427.

Schreier, H.W., Garcia, D. and Sutton, M.A. (2004), "Advances in light microscope stereo vision", *Exper. Mech.*, **44**, 278-288.

Sozen, S. (2015), "Determination of displacement distributions in welded steel tension elements using digital image techniques", *Steel Compos. Struct.*, **18**(5), 1103-1117.

Stanford, B., Ifju, P., Albertani, R. and Shyy, W. (2008), "Fixed membrane wings for micro air vehicles: Experimental characterization, numerical modeling, and tailoring", *Progr. Aerosp. Sci.*, **44**, 258-294.

Sutton, M.A., Wolters, W.J., Peters, W.H., Ranson, W.F. and McNeill, S.R. (1983), "Determination of displacements using an improved digital correlation method", *Image Vis. Comput.*, **1**, 133-139.

Vialettes, P., Siguier, J.M., Guigue, P., Karama, M., Mistou, S., Dalverny, O., Granier, S. and Petitjean, F. (2006), "Experimental and numerical simulation of super-pressure balloon apex section: Mechanical behavior in realistic flight conditions", *Adv. Space Res.*, **37**(11), 2082-2086.